

Cite this: *Energy Adv.*, 2022,  
1, 169Received 27th October 2021,  
Accepted 26th January 2022

DOI: 10.1039/d1ya00038a

rsc.li/energy-advances

# Enhanced photocatalytic activity of brown $\text{H}_4\text{Nb}_6\text{O}_{17}/\text{g-C}_3\text{N}_4$ composite for visible-light driven $\text{H}_2\text{O}_2$ production†

Luona Zhang,<sup>a</sup> Shiqi Zhao,<sup>a</sup> Xiaorong Cheng,<sup>b</sup> Zijie Liu,<sup>a</sup> Ruochen Liu<sup>a</sup> and  
Graham Dawson \*<sup>a</sup>

A novel form of brown  $\text{H}_4\text{Nb}_6\text{O}_{17}$  was synthesised by annealing niobate nanoscrolls at 300 °C. A composite heterojunction between this brown niobate and  $\text{g-C}_3\text{N}_4$  was formed, and shown to have enhanced photocatalytic activity for the ORR and  $\text{H}_2\text{O}_2$  production of 1.8  $\mu\text{mol}$  after 3 hours. The formation of a heterojunction between the two components was shown to alter the chemical environment and suppress the PL signal, and a band diagram of the system is proposed based on our results.

## 1. Introduction

The global energy crisis has solicited a widespread decarbonization imperativeness pushing for the advancement of clean energy conversion processes. Solar-driven photocatalytic production of  $\text{H}_2\text{O}_2$  has emerged as one of the most attractive solutions in the past decade. According to a large body of research,  $\text{H}_2\text{O}_2$  has arisen not only as a strong oxidant for organic pollutant degradation but also as an alternative fuel cell energy carrier to hydrogen gas ( $\text{H}_2$ ).<sup>1,2</sup> This solar fuel can be used in the design of advanced one-compartment cells with theoretical energy density close to that of two-compartment  $\text{H}_2$ -based fuel cells, and aqueous  $\text{H}_2\text{O}_2$  can be stored and transported more conveniently and safely than compressed  $\text{H}_2$ .<sup>3–5</sup> At present, commercial-scale synthesis of  $\text{H}_2\text{O}_2$  involves the anthraquinone oxidation process, also called the Riedl–Pfleiderer process, which is a hazardous method with intensive consumption of energy and organic solvents.<sup>6,7</sup> Therefore, the development of cost-effective, efficient photocatalytic routes to synthesize  $\text{H}_2\text{O}_2$  *via* the oxygen reduction reaction (ORR) is in great demand.

Among semiconductor photocatalysts, niobium oxides (*e.g.*,  $\text{KNbO}_3$ ,  $\text{K}_4\text{Nb}_6\text{O}_{17}$ ) have attracted much attention as promising candidates.  $\text{K}_4\text{Nb}_6\text{O}_{17}$  has a unique structure, consisting of stacked asymmetrical negatively-charged  $\text{Nb}_6\text{O}_{17}^{4-}$  lamellas with edge- and corner-shared  $\text{NbO}_6$  octahedra and interlayer regions occupied by the alkaline cations.<sup>8,9</sup> In the

study conducted by Zhou *et al.*, porous  $\text{K}_4\text{Nb}_6\text{O}_{17}$  microspheres exhibit good activity for the degradation of the organic dye Rhodamine B, two times higher than that of the commercial Degussa P25  $\text{TiO}_2$ .<sup>10</sup> Similarly, Li *et al.* demonstrate that nanostructuring of niobates greatly benefit the specific surface area, triggering enormous improvements to the photocatalytic activity.<sup>11</sup> Further to this point, research work on niobate nanotubes can be still considered in its infancy, and several enhancement techniques yet remain to be tested. To this end, we investigated the impact of the annealing treatment, carried out to potentially induce useful chemo-physical alterations. We postulate that the structure of proton-exchanged  $\text{H}_4\text{Nb}_6\text{O}_{17}$  is subject to partial destruction of the tubes during the annealing treatment, which results in incorporation of the interlayer exfoliating agent within the tube interlayers. This feature bestows the resulting brown niobate with interesting optical properties. However, major constraints on its photocatalytic performance, including the inadequate solar spectrum absorption and recombination of photogenerated charge carriers, entails the necessity of additional aid from secondary species.

A wide array of synergistic strategies has been successfully applied to alter the properties of transition metal oxides, such as surface modification using organic compounds and composite construction. For instance, Liu *et al.* found that catechol coatings selectively generate a signal in the surface-enhanced Raman scattering of trititanate nanotubes (TiNT).<sup>12</sup> Also, the construction of a heterojunction with secondary species has been proven to be significant to boost the solar-to-fuel conversion efficiency. In fact, mixing two components at the nano-scale provides strong interfacial interaction, improving thus the charge carrier dynamics. For example, Wu *et al.* and Tan *et al.* both report  $\text{g-C}_3\text{N}_4/\text{TiO}_2$  heterojunctions showing a lower recombination rate and enhanced photocatalytic activity.<sup>13,14</sup>

<sup>a</sup> Department of Chemistry, Xi'an Jiaotong Liverpool University, Suzhou, Jiangsu, 215123, P. R. China. E-mail: graham.dawson@xjtlu.edu.cn

<sup>b</sup> Suzhou Vocational Institute of Industrial Technology, Suzhou, Jiangsu, 215104, P. R. China

† Electronic supplementary information (ESI) available: Further XRD, UV/vis spectra; valence band edge spectra. See DOI: 10.1039/d1ya00038a



Recently, polymeric  $g\text{-C}_3\text{N}_4$  has been extensively studied because of its versatility and metal-free 2D structure. First reported as a photocatalyst by Wang *et al.*, it is earth-abundant, thermally stable, and can be easily fabricated from nitrogen-rich precursors (*e.g.* urea, thiourea, melamine and cyanamide).<sup>15,16</sup> More importantly, it exhibits appropriate band levels for visible light absorption with a bandgap of approx. 2.7 eV. However, this material is still far from optimum given the presence of critical shortcomings: weak exciton dissociation, poor charge carrier mobility and high recombination rate.<sup>15,17</sup> Nevertheless, combining  $\text{H}_4\text{Nb}_6\text{O}_{17}$  and  $g\text{-C}_3\text{N}_4$  ensures appropriate surface contact which can greatly promote mutual charge transfer. To the best of our knowledge, few attempts have been made to modify nanostructured  $\text{H}_4\text{Nb}_6\text{O}_{17}$  by either the adsorption or intercalation of  $g\text{-C}_3\text{N}_4$  in the interlayer regions.

Herein, we discuss the profound effect of the annealing treatment on pristine  $\text{H}_4\text{Nb}_6\text{O}_{17}$ . Thus, a novel phase of niobate was found and characterized. Its unique absorption profile and surface bonding are particularly fascinating and, therefore, have been thoroughly investigated. Moreover, this study firstly reports a heterojunction between annealed  $\text{H}_4\text{Nb}_6\text{O}_{17}$  nanotubes and  $g\text{-C}_3\text{N}_4$  with superior ORR performance under visible light irradiation. Specifically, the photocatalytic activity of the as-prepared composite was evaluated by quantifying the photo-generated  $\text{H}_2\text{O}_2$  in an aqueous solution. Composite-construction provides a suitable band structure and close affiliation between the components for improving the charge separation. The charge transport pathway and a possible mechanism for the photocatalytic reduction of  $\text{O}_2$  to  $\text{H}_2\text{O}_2$  over the hybrid catalyst are also proposed.

## 2. Experimental section

### 2.1 Preparation of photocatalysts

Pristine  $g\text{-C}_3\text{N}_4$  was obtained *via* pyrolysis of urea under ambient pressure without additive assistance. The precursor urea

was placed in a covered crucible and then calcinated at  $550\text{ }^\circ\text{C}$  for 4 h.<sup>18</sup>

The precursor  $\text{K}_4\text{Nb}_6\text{O}_{17}$  was synthesized by heating a mixture of  $\text{Nb}_2\text{O}_5$  and  $\text{K}_2\text{CO}_3$  with a defined stoichiometric ratio of 3 : 2 at  $1100\text{ }^\circ\text{C}$  for 24 h. The as-obtained  $\text{K}_4\text{Nb}_6\text{O}_{17}$  powder was washed with deionized water and dried at  $80\text{ }^\circ\text{C}$  for 3 h.  $\text{K}_4\text{Nb}_6\text{O}_{17}$  was then subject to a proton exchange process to substitute the  $\text{K}^+$  cations with protons. 1.15 g  $\text{K}_4\text{Nb}_6\text{O}_{17}$  was suspended in 30 mL 6 M  $\text{HNO}_3$  aqueous solution and stirred with a rate of 550 rpm at  $60\text{ }^\circ\text{C}$  for 7 days. The product  $\text{H}_4\text{Nb}_6\text{O}_{17}$  was then recovered by vacuum filtration and dried at  $80\text{ }^\circ\text{C}$  for 1 h.

Niobate nanotubes were formed by the exfoliation action of tetrabutylammonium-hydroxide (TBA-OH) and subsequent scrolling. 1 g  $\text{H}_4\text{Nb}_6\text{O}_{17}$  powder was dispersed in deionized water, and 25% TBA-OH aqueous solution was added dropwise until the pH of the suspension was adjusted to 9.5–10. The dispersion was stirred at a rate of 600 rpm at  $45\text{ }^\circ\text{C}$  for 3 days. Finally, 1 M  $\text{HNO}_3$  was added drop-wise to the niobate dispersion until a pH between 1 and 2 was measured. The solid sample was washed with Milli-Q water using vacuum filtration and dried at  $60\text{ }^\circ\text{C}$  overnight. The product was annealed at  $300\text{ }^\circ\text{C}$  for 4 h with a heating rate of  $3\text{ }^\circ\text{C min}^{-1}$ .

The coupling process of  $\text{H}_4\text{Nb}_6\text{O}_{17}$  and  $g\text{-C}_3\text{N}_4$  was based on the surface charge-induced hetero-aggregation phenomenon, in which the electrostatic attraction between the species was promoted *via* mechanical mixing.  $g\text{-C}_3\text{N}_4$  and  $\text{H}_4\text{Nb}_6\text{O}_{17}$  were suspended in deionized water according to the ratio  $0.5\text{ mg mL}^{-1}$ . After being sonicated for 30 min, the niobate dispersion was transferred into a different flask, and  $g\text{-C}_3\text{N}_4$  was then poured slowly under magnetic stirring at 650 rpm. The mixing continued without interruptions for 3 hours. Finally, the mixture was washed with Milli-Q water using vacuum filtration and dried in the oven at  $80\text{ }^\circ\text{C}$  for one hour. The process is shown schematically in Fig. 1. More information on the optimisation of the composite is given in the ESI,<sup>†</sup> Section 2.

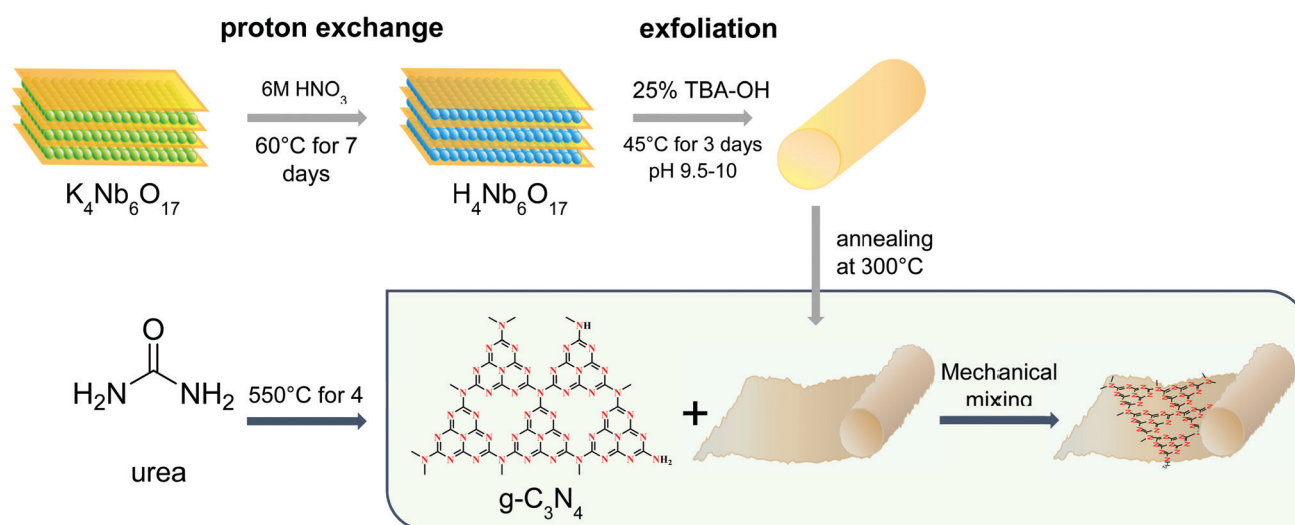


Fig. 1 Schematic representation of the reactions involved to prepare the composite materials.



## 2.2 Characterization

X-Ray diffraction (XRD) patterns were acquired on a Bruker D8 ADVANCE powder X-ray diffractometer with Cu-K $\alpha$  radiation, operating at 40 kV and 40 mA. Transmission electron microscopy (TEM) images were collected on a FEI Tecnai G2 F20 S-TWIN TMP microscope at an acceleration voltage of 200 kV. Fourier-transform infrared spectra were acquired on a Cary 660 FTIR spectrometer from Agilent Technologies. X-Ray photoelectron spectroscopic (XPS) analysis was performed using a Thermo Scientific ESCALAB 250 XI spectrometer. UV-visible spectra were measured with an Agilent Cary 300 spectrophotometer. Photoluminescence was measured using a Horiba LabRAM HR Raman spectrometer.

## 2.3 Photocatalytic oxygen reduction

H<sub>2</sub>O<sub>2</sub> was synthesized *via* photocatalytic reduction of molecular oxygen under visible light irradiation ( $\lambda > 400$  nm) using a 300 W Xe lamp with a 400 nm cutoff filter as the light source. 0.100 g of catalyst was uniformly dispersed in 100 mL of aqueous solution containing 5 vol% methanol according to a ratio of 1 g L<sup>-1</sup>. The suspension was sonicated for 10 min and transferred in a quartz photoreactor, which was connected to a circulating water system to remove the thermal effect of light. While O<sub>2</sub> was continually bubbled through the suspension, the system was stirred in the dark for 2 hours to ensure the adsorption-desorption equilibrium among the catalyst, dissolved O<sub>2</sub> and water. During the irradiation, the reaction temperature was kept at 20 °C. At given time intervals, 1.5 mL aliquots were collected and filtered to separate the liquid samples from the solid catalyst. The amount of H<sub>2</sub>O<sub>2</sub> was measured by iodometric titration.

## 3. Results and discussion

### 3.1 Crystallinity and morphology

The XRD patterns of the samples were used to investigate their crystalline structure. As shown in Fig. 2, the main peaks of K<sub>4</sub>Nb<sub>6</sub>O<sub>17</sub> can be found at 4.73° and 9.41°, which match well with the (020) and (040) crystal planes of pure orthorhombic

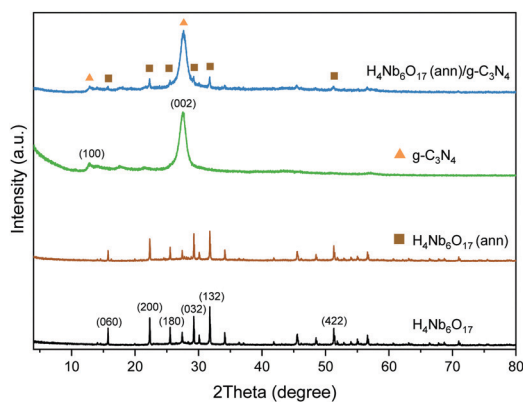


Fig. 2 XRD patterns of the as-prepared H<sub>4</sub>Nb<sub>6</sub>O<sub>17</sub> before and after annealing at 300 °C and g-C<sub>3</sub>N<sub>4</sub> and their composites samples.

K<sub>4</sub>Nb<sub>6</sub>O<sub>17</sub> (JCPDS, No. 76-0977 and Fig. S1, ESI<sup>†</sup>).<sup>11</sup> As a result of the subsequent proton exchange and exfoliation treatment, the layered structure was demolished, causing the related peaks to disappear. The remaining peaks of the exfoliated H<sub>4</sub>Nb<sub>6</sub>O<sub>17</sub> are observed at 15.74°, 22.31°, 29.25° and 31.76°, corresponding to the (060), (200), (032) and (132) crystal planes. The annealing process at 300 °C does not affect the crystalline structure of H<sub>4</sub>Nb<sub>6</sub>O<sub>17</sub>, and the same diffraction peaks were detected without distinguishable variations in the relative intensity.

The (100) and (002) crystal planes of g-C<sub>3</sub>N<sub>4</sub> exhibit their characteristic peaks at 12.79° and 27.52°. The first is associated with the in-plane repeating units of the continuous heptazine framework, and the second is related to the stacking of the conjugated aromatic structure around the *c*-axis.<sup>19</sup> The respective *d*-spacing values are equal to 0.692 nm and 0.324 nm, which are consistent with the reported lengths.<sup>16,18,19</sup> The H<sub>4</sub>Nb<sub>6</sub>O<sub>17</sub> (ann)/g-C<sub>3</sub>N<sub>4</sub> composite possesses the typical peaks of both components with a clear overlapping because of the higher amount of g-C<sub>3</sub>N<sub>4</sub>.

The morphology of the photocatalysts was observed by TEM. The H<sub>4</sub>Nb<sub>6</sub>O<sub>17</sub> nanotubes can be observed in Fig. 3a and b. The

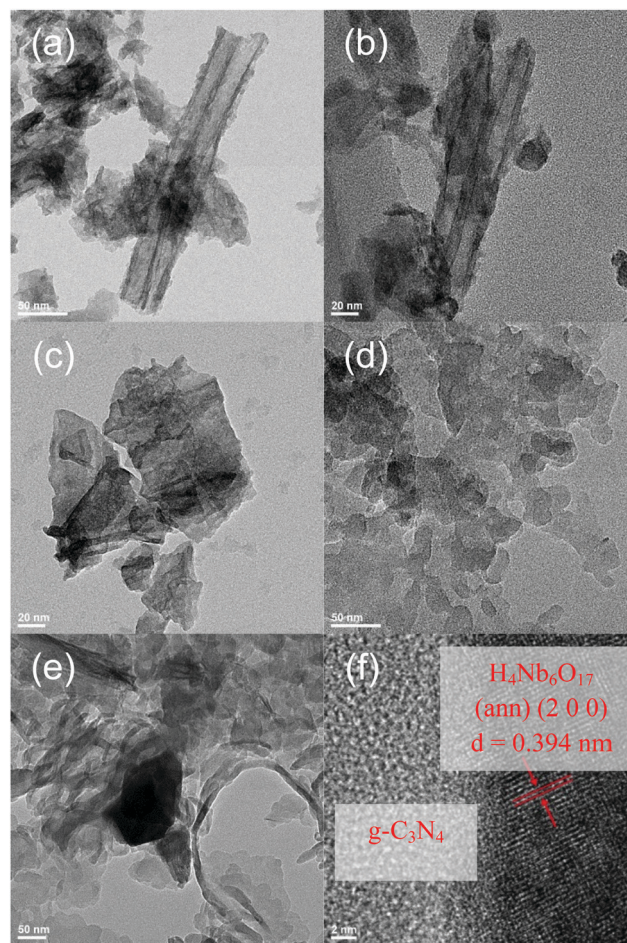


Fig. 3 TEM images of (a and b) H<sub>4</sub>Nb<sub>6</sub>O<sub>17</sub>, (c) H<sub>4</sub>Nb<sub>6</sub>O<sub>17</sub> (ann) and (d) g-C<sub>3</sub>N<sub>4</sub>. (e) TEM and (f) HRTEM images of the H<sub>4</sub>Nb<sub>6</sub>O<sub>17</sub> (ann)/g-C<sub>3</sub>N<sub>4</sub> composite.





scrolled tubular structure, which results from the exfoliation and scrolling of the niobate sheets,<sup>20</sup> incorporating the TBAO-between the layers. The annealing treatment provokes a dramatic increase in the degree of aggregation as well as a substantial degradation of the tubular structure (Fig. 3b and c, schematically in Fig. 1).

In great contrast to  $\text{H}_4\text{Nb}_6\text{O}_{17}$ , untreated carbon nitride has an amorphous and irregular 3-dimensional disposition as well as a bulky structure (Fig. 3d). Moreover, the low crystallinity prevents the formation of obvious lattice fringes. These features are expected to hinder light absorption, charge transport and mass transportation. On the other hand, the observed porosity can increase the specific surface area, and more active sites might lead to greater photocatalytic activity. This is supported by the BET surface area results, shown in Fig. S2 (ESI<sup>†</sup>). The composite displays a type IV hysteresis according to the IUPAC classification with H3 type hysteresis loops for both components and composites, suggesting their mesoporous nature with aggregates of plate-like particles and irregular slit-shaped pores.

In Fig. 3e, the TEM image of the  $\text{H}_4\text{Nb}_6\text{O}_{17}$  (ann)/ $\text{g-C}_3\text{N}_4$  (1:10) composite is displayed, evidencing that  $\text{H}_4\text{Nb}_6\text{O}_{17}$  nanostructures have been anchored on the surface of  $\text{g-C}_3\text{N}_4$ . Fig. 3f confirms the coexistence of  $\text{H}_4\text{Nb}_6\text{O}_{17}$  nanostructures and  $\text{g-C}_3\text{N}_4$ , and the lattice spacing of 0.394 nm is consistent with the (200) plane of  $\text{H}_4\text{Nb}_6\text{O}_{17}$  (ann). These results provide evidence of the successful formation of a heterojunction in the  $\text{H}_4\text{Nb}_6\text{O}_{17}$  (ann)/ $\text{g-C}_3\text{N}_4$  composite. The electrostatic interaction between the components is indicated by the zeta potential results, shown in Fig. S3 (ESI<sup>†</sup>).

### 3.2 Optical absorption

The optical absorption ability of the as-prepared samples was investigated using UV-visible absorption spectra, shown in Fig. 4.  $\text{H}_4\text{Nb}_6\text{O}_{17}$  shows no absorption of visible light and holds the same absorption profile as  $\text{K}_4\text{Nb}_6\text{O}_{17}$ , as reported by Tian *et al.*,<sup>21</sup> with the main absorption edge at 372 nm. Meanwhile,  $\text{g-C}_3\text{N}_4$  has a sharp absorption edge at 447 nm with the

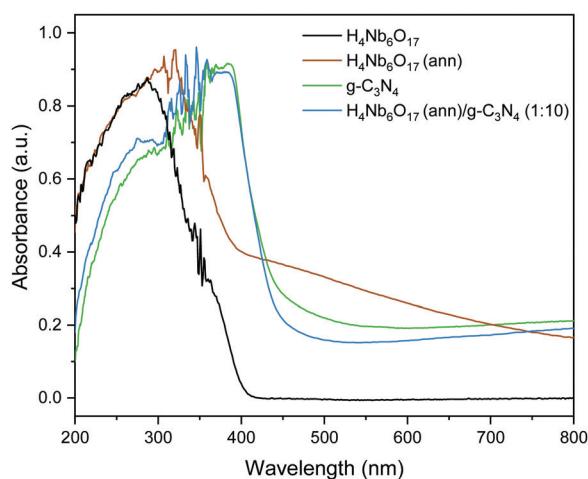


Fig. 4 UV/vis spectra of the samples.

maximum absorption at 390 nm, in good accordance with previous reports.<sup>22,23</sup>

Furthermore, it can be observed that the annealing treatment (at 300 °C) substantially impacted the absorption profile of  $\text{H}_4\text{Nb}_6\text{O}_{17}$ , as hinted by the distinctive change in the powder colouring from white to brown. The peak of highest absorption exhibits a red shift, and a broad shoulder-like curve stretches through the visible-light region. This shoulder is ascribed to charge transfer between the niobate and the organic material within the tubular structure after annealing, in accordance with our previous work on organic surface modification of nanostructures.<sup>24</sup> According to the Kubelka–Munk plots, shown in Fig. S4, (ESI<sup>†</sup>) the calculated bandgaps of  $\text{g-C}_3\text{N}_4$ ,  $\text{H}_4\text{Nb}_6\text{O}_{17}$  and  $\text{H}_4\text{Nb}_6\text{O}_{17}$  (ann) are 2.82, 3.44 and 3.01 eV, respectively. Because of the dominating presence of  $\text{g-C}_3\text{N}_4$ , the absorption spectrum of the  $\text{H}_4\text{Nb}_6\text{O}_{17}$  (ann)/ $\text{g-C}_3\text{N}_4$  (1:10) composite replicates the response of this component, without showing relevant differences, and a calculated band gap of 2.87 eV. The UV/vis spectra of  $\text{H}_4\text{Nb}_6\text{O}_{17}$  annealed at different temperatures is shown in Fig. S5 (ESI<sup>†</sup>).

### 3.3 FT-IR

The FT-IR spectra of the samples are displayed in Fig. 5.  $\text{H}_4\text{Nb}_6\text{O}_{17}$  exhibits broad bands in the range 400–1000  $\text{cm}^{-1}$  due to the vibrational modes of octahedral  $\text{NbO}_6$ .<sup>11</sup> The annealed sample retains these characteristic peaks, indicating an unvaried chemical composition after the annealing process. In the  $\text{g-C}_3\text{N}_4$  sample, the peaks between 1200 and 1700  $\text{cm}^{-1}$  are typical absorption bands, related to the skeletal stretching of C–N heterocycles.<sup>22</sup> Furthermore, the peak at 816  $\text{cm}^{-1}$  is associated to the breathing vibrations of triazine units, and the broad band between 3000 and 3400  $\text{cm}^{-1}$  is ascribed to either –NH or –OH stretching vibrations. The  $\text{H}_4\text{Nb}_6\text{O}_{17}$  (ann)/ $\text{g-C}_3\text{N}_4$  (1:10) composite exhibits all the peaks as pristine  $\text{g-C}_3\text{N}_4$ .

### 3.4 Raman

Additionally, Raman spectra were collected to further study the annealing effect on the skeletal structure of  $\text{H}_4\text{Nb}_6\text{O}_{17}$ , shown in Fig. 6. Several new peaks are observed and the two main peaks in the original niobate sample are shifted. New peaks are

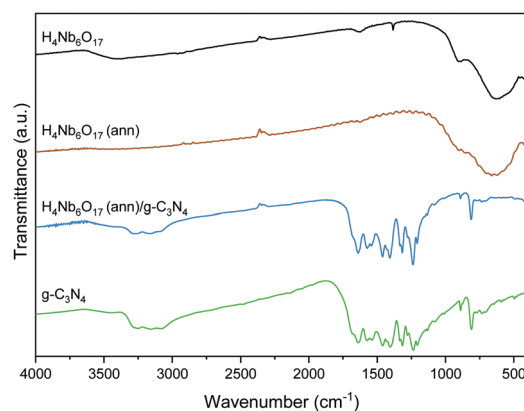


Fig. 5 FTIR spectra of the samples.



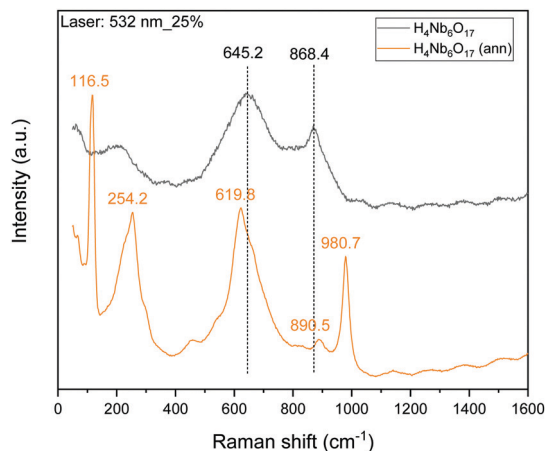


Fig. 6 Raman spectra of  $\text{H}_4\text{Nb}_6\text{O}_{17}$  before and after annealing.

observed at 116.5 and 254.2  $\text{cm}^{-1}$ , which are characterized as bending modes of  $\text{NbO}_6$  octahedral units.<sup>11</sup> However, the strongest characteristic band located at 645  $\text{cm}^{-1}$ , corresponding to the stretching vibrations of the longer Nb–O bond in the  $\text{NbO}_6$  octahedral units, is blue-shifted to 619.80  $\text{cm}^{-1}$ .<sup>25</sup> Moreover, the peak at 868.4 is slightly red-shifted to 890.5  $\text{cm}^{-1}$  which is associated to stretching modes of the shorter Nb–O terminal group resulting from the replacement of  $\text{K}^+$  with  $\text{H}_3\text{O}^+$ . A new peak at 980.7  $\text{cm}^{-1}$  is also observed after annealing. The three newly observed peaks are indicative of the incorporation of the organic exfoliating agent into the niobate structure.

### 3.5 XPS

A deeper study of the interaction between the species was then provided by XPS analysis to investigate the surface composition and chemical states of the as-prepared samples. Specimen charge was referenced to the C 1s peak of adventitious hydrocarbon, which is assumed to have a binding energy of 284.8 eV. As displayed in the survey spectra (Fig. 7a),  $\text{H}_4\text{Nb}_6\text{O}_{17}$  contains the elements Nb and O with a small contamination of adventitious carbon. The overall elemental composition was retained in the annealed sample. However, important differences can be observed in the high-resolution XPS measurements. Furthermore, compared to the spectrum of  $\text{H}_4\text{Nb}_6\text{O}_{17}$  (ann), the composite shows distinct signals of C 1s and N 1s due to the introduction of  $\text{g-C}_3\text{N}_4$ , demonstrating that the two materials were successfully coupled.

In the Nb 3d spectrum of  $\text{H}_4\text{Nb}_6\text{O}_{17}$  (Fig. 7b), two typical peaks can be observed at 206.97 and 209.72 eV with a peak area ratio of 3:2 due to the spin-orbital splitting into Nb 3d<sub>5/2</sub> and Nb 3d<sub>3/2</sub>, respectively.<sup>26,27</sup> The Nb<sup>5+</sup>–O bond is also responsible for the peak at 530.10 eV in the O 1s spectrum, while the broad peak at 531.15 eV could be ascribed to surface-adsorbed oxygen species (Fig. 7c). The annealing process of  $\text{H}_4\text{Nb}_6\text{O}_{17}$  at 300 °C induces a noticeable shift of approx. 0.2 eV towards higher binding energies in both O 1s and Nb 3d spectra. This means that, despite the preservation of the same crystalline structure and composition, the annealed  $\text{H}_4\text{Nb}_6\text{O}_{17}$  possesses

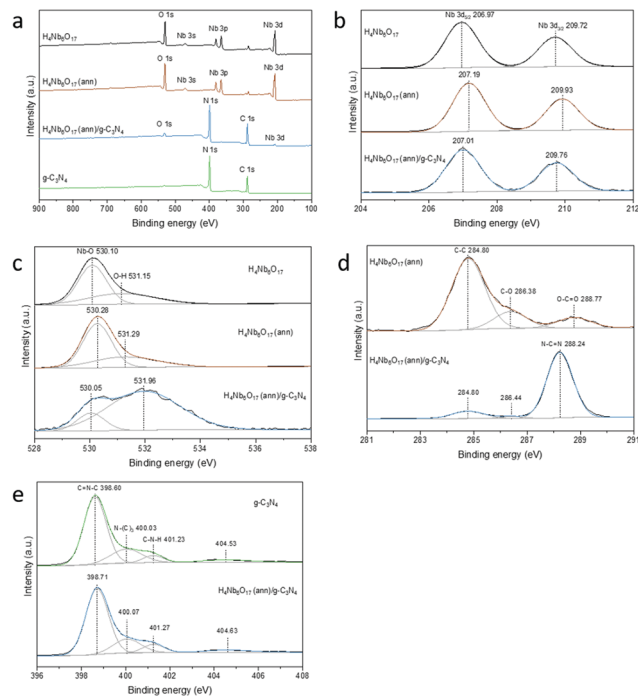


Fig. 7 XPS survey spectrum (a), Nb 3d (b), 1s (c), C 1s (d) and N 1s (e) spectra of  $\text{H}_4\text{Nb}_6\text{O}_{17}$  before and after annealing and  $\text{H}_4\text{Nb}_6\text{O}_{17}$  (ann)/ $\text{g-C}_3\text{N}_4$  composite samples.

remarkable differences in terms of intramolecular and intermolecular interactions that are worth further investigation.

The coupling process with  $\text{g-C}_3\text{N}_4$  also changes the surface electron density in the heterojunction photocatalyst.<sup>28</sup> The characteristic peaks of Nb 3d shifted to lower binding energies compared to those of  $\text{H}_4\text{Nb}_6\text{O}_{17}$  (ann). However, the spin–orbit separation value between Nb 3d<sub>5/2</sub> and Nb 3d<sub>3/2</sub> did not change from  $\text{H}_4\text{Nb}_6\text{O}_{17}$  to  $\text{H}_4\text{Nb}_6\text{O}_{17}$  (ann)/ $\text{g-C}_3\text{N}_4$ , indicating the exclusive presence of Nb<sup>5+</sup>.<sup>29</sup> Similarly, the distinct peak corresponding to the lattice oxygen in the O 1s spectrum, significantly shifted to lower binding energies. Moreover, the new peak at 531.96 eV could suggest the formation of C=O bonds between  $\text{H}_4\text{Nb}_6\text{O}_{17}$  (ann) and  $\text{g-C}_3\text{N}_4$ .<sup>28</sup>

As shown in Fig. 7d for the C 1s spectrum, the  $\text{H}_4\text{Nb}_6\text{O}_{17}$  (ann) sample shows a weak signal for the characteristic bonds of adventitious carbon, which are reproduced in the  $\text{H}_4\text{Nb}_6\text{O}_{17}$  (ann)/ $\text{g-C}_3\text{N}_4$  composite. Additionally, the profile of the composite clearly inherited the major peak associated with the sp<sup>2</sup>-bonded carbon of the s-triazine rings in  $\text{g-C}_3\text{N}_4$  (N–C=N).<sup>30</sup> The N 1s spectra of both  $\text{g-C}_3\text{N}_4$  and  $\text{H}_4\text{Nb}_6\text{O}_{17}$  (ann)/ $\text{g-C}_3\text{N}_4$  are deconvoluted into three peaks, shown in Fig. 7d. The first can be assigned to the sp<sup>2</sup>-bonded nitrogen (C=N–C), the second is related to the tertiary nitrogen groups N–(C)<sub>3</sub> and the third belongs to the amino groups (C–N–H).<sup>26,31</sup> One additional band centred at approx. 404.7 eV might correspond to  $\pi$ -excitations and charging effects. All of them slightly shifted toward higher binding energies after the coupling process because of a different chemical environment, indicating the formation of a heterojunction. This is consistent with the TGA results



(Fig. S6, ESI<sup>†</sup>), which indicate the incorporation of a small percentage of organic material in the annealed compound. From these results we propose that the annealing of the niobate tubular material at 300 °C causes stronger incorporation of the organic intercalation into the layer,<sup>32</sup> and partial unscrolling of the tubular structure, resulting in the shoulder in the UV/vis.

### 3.6 ORR performances

The photocatalytic H<sub>2</sub>O<sub>2</sub> production over the series of photocatalysts under visible light irradiation was evaluated with methanol as sacrificial agent. As shown in Fig. 8, no H<sub>2</sub>O<sub>2</sub> was formed over H<sub>4</sub>Nb<sub>6</sub>O<sub>17</sub> while the annealed sample (300 °C) revealed a slight H<sub>2</sub>O<sub>2</sub> production ability. This difference could be easily justified by the fact that the annealed H<sub>4</sub>Nb<sub>6</sub>O<sub>17</sub> moderately absorbs in the visible range in contrast to the pristine form. For the same reason, graphitic carbon nitride, which has a narrow bandgap falling in the visible region, was able to efficiently generate H<sub>2</sub>O<sub>2</sub> with a steady increase over 2.5 hours. Among all the samples, the H<sub>4</sub>Nb<sub>6</sub>O<sub>17</sub> (ann)/g-C<sub>3</sub>N<sub>4</sub> composite exhibited the highest H<sub>2</sub>O<sub>2</sub> production. This superior photocatalytic ORR performance can be ascribed to the enhanced charge separation efficiency.

Additionally, the ORR experiment was repeated without a photocatalyst or in the dark, and no H<sub>2</sub>O<sub>2</sub> was generated throughout the whole time interval. These results confirm that any amount of H<sub>2</sub>O<sub>2</sub> produced is directly associated to the presence of a photocatalyst and to its specific activity upon visible light irradiation, denoting the decisive role of photocatalysis in the O<sub>2</sub> reduction process. The long term stability of the photocatalysts was investigated by recycling tests. The results are shown in Fig. S7 (ESI<sup>†</sup>).

### 3.7 PL

The charge carrier dynamics was studied using photoluminescence spectra. PL spectra were acquired under 325 nm excitation at room temperature to evaluate the ability of the samples to hold the absorbed photoenergy and direct it towards photocatalytic routes. As shown in Fig. 9, the major emission peak of g-C<sub>3</sub>N<sub>4</sub> is centred at approx. 470 nm, and is assigned to the n-π\*

electron transitions of the lone pair electrons on the nitrogen atom.<sup>3</sup> The PL intensity of the H<sub>4</sub>Nb<sub>6</sub>O<sub>17</sub> (ann)/g-C<sub>3</sub>N<sub>4</sub> composite is decreased by approx. 40% compared to pristine g-C<sub>3</sub>N<sub>4</sub>, and the signal was red-shifted by approx. 25 nm. This significant quenching demonstrates a more efficient charge separation with equal absorption ability.

### 3.8 Photocatalytic mechanism and band diagram

Based on the aforementioned results and references, a mechanism for the photocatalytic reduction of O<sub>2</sub> to H<sub>2</sub>O<sub>2</sub> by the hybrid catalysts is proposed. In addition, the VB-XPS spectra were employed to determine the valence band energies. As depicted in Fig. S8, (ESI<sup>†</sup>) the valence band positions of g-C<sub>3</sub>N<sub>4</sub> and H<sub>4</sub>Nb<sub>6</sub>O<sub>17</sub> (ann) are estimated at 2.10 and 2.72 eV, respectively. Therefore, the corresponding conduction band potentials are -0.72 and -0.29 eV vs. NHE, according to the equation:  $\Delta E_g = |E_{CB} - E_{VB}|$ . The resulting band alignment within the H<sub>4</sub>Nb<sub>6</sub>O<sub>17</sub> (ann)/g-C<sub>3</sub>N<sub>4</sub> composite, displayed in Fig. 10, follows the staggered gap model.

A possible charge transfer pathways is also illustrated. Upon visible light irradiation, both components are activated and undergo exciton dissociation. The band discontinuity between the CB levels of the two components is narrow, favouring the formation of an interfacial channel for charge transfer.<sup>33,34</sup> Suppression of PL intensity and increasing photocatalytic activities specifically support this trend. Therefore, photogenerated electrons accumulate in the CB of the annealed H<sub>4</sub>Nb<sub>6</sub>O<sub>17</sub>, while positively-charged holes of the niobate component tend to migrate to the VB of g-C<sub>3</sub>N<sub>4</sub> because of its less positive potential. The annealed H<sub>4</sub>Nb<sub>6</sub>O<sub>17</sub> also benefits from the presence of sub-band states due to the shoulder in the visible region, indicating the possibility of additional charge transfer pathways. The improved separation of the charge carriers is the major factor promoting a superior H<sub>2</sub>O<sub>2</sub> production performance for the hybrid photocatalyst.

Moreover, the band levels of both g-C<sub>3</sub>N<sub>4</sub> and H<sub>4</sub>Nb<sub>6</sub>O<sub>17</sub> have straddled the potential difference for O<sub>2</sub>/H<sub>2</sub>O<sub>2</sub> (0.69 V vs. NHE). Photoinduced electrons transfer to the photocatalyst surface to participate in the reduction of molecular oxygen. Meanwhile, the holes are consumed by the electron donor (methanol).

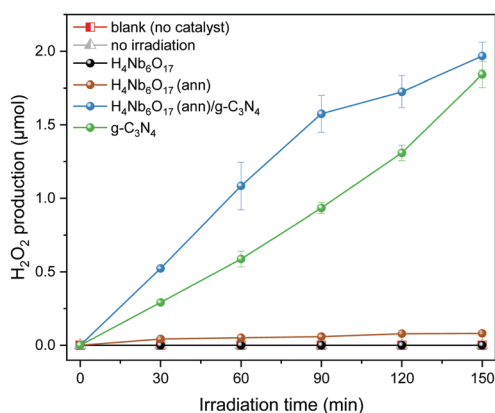


Fig. 8 Time-dependent photocatalytic H<sub>2</sub>O<sub>2</sub> production of the samples under visible light irradiation.

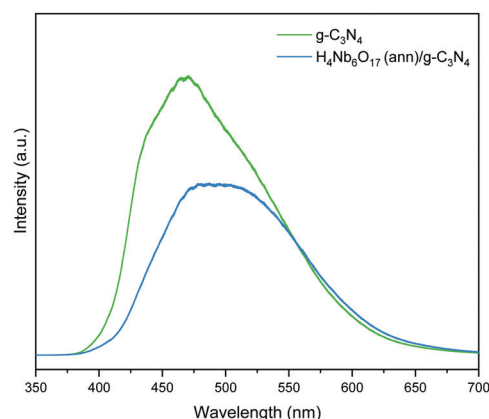


Fig. 9 PL spectra of g-C<sub>3</sub>N<sub>4</sub> and the H<sub>4</sub>Nb<sub>6</sub>O<sub>17</sub> (ann)/g-C<sub>3</sub>N<sub>4</sub> composite.



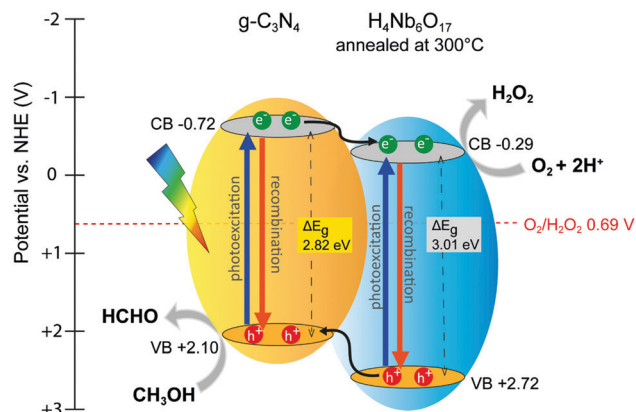


Fig. 10 Schematic illustration of the band levels and charge transfer pathways in the  $\text{H}_4\text{Nb}_6\text{O}_{17}$  (ann)/ $\text{g-C}_3\text{N}_4$  composite.

Thus, water oxidation is prevented by using a hole scavenger, so only two-electron or multi-step single-electron  $\text{O}_2$  reduction is a possible photocatalytic pathway for  $\text{H}_2\text{O}_2$  production. Fig. S9 (ESI<sup>†</sup>) shows the VB-XPS of  $\text{H}_4\text{Nb}_6\text{O}_{17}$  (ann)/ $\text{g-C}_3\text{N}_4$  composite, revealing an increase of 0.2 eV from the valence band maximum of  $\text{g-C}_3\text{N}_4$ . The down-shift of the valence band is believed to enhance the hole oxidation activity, affecting thus the overall photocatalytic activity by inhibiting the recombination phenomenon.<sup>35</sup>

We investigated the formation of radical species in  $\text{H}_4\text{Nb}_6\text{O}_{17}$  (ann)/ $\text{g-C}_3\text{N}_4$  and  $\text{g-C}_3\text{N}_4$  samples using electron paramagnetic resonance (EPR) spectroscopy in the presence of a 5,5-dimethyl-pyrroline-*N*-oxide (DMPO) spintrap in methanol under full range illumination, shown in Fig. S10 (ESI<sup>†</sup>). The six characteristic peaks of the DMPO  $\cdot\text{O}_2^-$  adduct were observed<sup>36,37</sup> after 2 min irradiation indicating the formation of superoxide radicals in the ORR process.

## 4. Conclusions

A composite of novel brown niobate and  $\text{g-C}_3\text{N}_4$  was synthesized and found to be active in the visible light induced ORR to produce  $\text{H}_2\text{O}_2$ . Brown niobate was formed by annealing nanoscrolls  $\text{H}_4\text{Nb}_6\text{O}_{17}$  at 300 °C, resulting in the incorporation of organic material and unscrolling of the tubes. The formation of a heterojunction between the two components was shown to alter the chemical environment and suppress the PL signal by hindering the annihilation of photoexcited electron-hole pairs. Based on these results, a band diagram is proposed.

## Author contribution

L. Z. – data curation; investigation; formal analysis; writing – original draft; S. Z., Z. L., R. L. – data acquisition; X. C. – conceptualization; G. D. – conceptualization, project administration, supervision; writing – review and editing.

## Conflicts of interest

There are no conflicts to declare.

## Acknowledgements

This work was supported by Suzhou Institute of Industrial Technology Research Fund (Grant No. SGYKJ201705 and 2017kyqd010), Xi'an Jiaotong Liverpool University Research Development Fund and Key Programme Special Fund in XJTLU (KSF-E-02). National Natural Science Foundation of China (Grant No. 21650110446).

## References

- 1 S. Hu, X. Sun, Y. Zhao, W. Li, H. Wang and G. Wu, *J. Taiwan Inst. Chem. Eng.*, 2020, **107**, 129–138.
- 2 S. Zhao and X. Zhao, *J. Catal.*, 2018, **366**, 98–106.
- 3 Z. Wei, M. Liu, Z. Zhang, W. Yao, H. Tan and Y. Zhu, *Energy Environ. Sci.*, 2018, **11**, 2581–2589.
- 4 Y. Yang, Z. Zeng, G. Zeng, D. Huang, R. Xiao, C. Zhang, C. Zhou, W. Xiong, W. Wang, M. Cheng, W. Xue, H. Guo, X. Tang and D. He, *Appl. Catal., B*, 2019, **258**, 117956.
- 5 T. Baran, S. Wojtyła, A. Vertova, A. Minguzzi and S. Rondinini, *J. Electroanal. Chem.*, 2018, **808**, 395–402.
- 6 M. Teranishi, R. Hoshino, S. Naya and H. Tada, *Angew. Chem., Int. Ed.*, 2016, **55**, 12773–12777.
- 7 X. Zeng, Y. Liu, Y. Kang, Q. Li, Y. Xia, Y. Zhu, H. Hou, M. H. Uddin, T. R. Gengenbach, D. Xia, C. Sun, D. T. McCarthy, A. Deletic, J. Yu and X. Zhang, *ACS Catal.*, 2020, **10**, 3697–3706.
- 8 M. A. Bizeto and V. R. L. Constantino, *Mater. Res. Bull.*, 2004, **39**, 1729–1736.
- 9 M. A. Bizeto, A. L. Shiguihara and V. R. L. Constantino, *J. Mater. Chem.*, 2009, **19**, 2512–2525.
- 10 C. Zhou, G. Chen and Q. Wang, *J. Mol. Catal. A: Chem.*, 2011, **339**, 37–42.
- 11 D. Li, Q. Li, J. He, L. Hu and J. Hu, *New J. Chem.*, 2016, **40**, 136–143.
- 12 R. Liu, E. Morris, X. Cheng, E. Amigues, K. Lau, B. Kim, Y. Liu, Z. Ke, S. E. Ashbrook, M. Bühl and G. Dawson, *ChemistrySelect*, 2018, **3**, 8338–8343.
- 13 X. Xu, L. Xiao, Y. Jia, Z. Wu, F. Wang, Y. Wang, N. O. Haugen and H. Huang, *Energy Environ. Sci.*, 2018, **11**, 2198–2207.
- 14 Y. Tan, Z. Shu, J. Zhou, T. Li, W. Wang and Z. Zhao, *Appl. Catal., B*, 2018, **230**, 260–268.
- 15 M. S. Nasir, G. Yang, I. Ayub, S. Wang, L. Wang, X. Wang, W. Yan, S. Peng and S. Ramakarishna, *Appl. Catal., B*, 2019, **257**, 117855.
- 16 X. Wang, M. Kazuhiko, T. Arne, K. Takanabe, X. Gang, J. M. Carlsson, K. Domen and M. Antonietti, *Nat. Mater.*, 2009, **8**, 76–80.
- 17 Y. Zheng, L. Lin, B. Wang and X. Wang, *Angew. Chem.*, 2015, **54**, 12868–12884.





- 18 J. Liu, T. Zhang, Z. Wang, G. Dawson and W. Chen, *J. Mater. Chem.*, 2011, **21**, 14398–14401.
- 19 L. Shi, L. Yang, W. Zhou, Y. Liu, L. Yin, X. Hai, H. Song and J. Ye, *Small*, 2018, **14**, 1703142.
- 20 M. C. Sarahan, E. C. Carroll, M. Allen, D. S. Larsen, N. D. Browning and F. E. Osterloh, *J. Solid State Chem.*, 2008, **181**, 1678–1683.
- 21 L. Tian, K. Sun, Y. Rui, W. Cui and W. An, *RSC Adv.*, 2018, **8**, 29309–29320.
- 22 F. Dong, L. Wu, Y. Sun, M. Fu, Z. Wu and S. C. Lee, *J. Mater. Chem.*, 2011, **21**, 15171–15174.
- 23 Q. Huang, J. Wang, P. Wang, H. Yao and Z. Li, *Int. J. Hydrogen Energy*, 2017, **42**, 6683–6694.
- 24 G. Dawson, J. Liu, L. Lu and W. Chen, *ChemCatChem*, 2012, **4**, 1133–1138.
- 25 C. Guo, J. Zhu, J. He, L. Hu, P. Zhang and D. Li, *Vacuum*, 2020, **182**, 109718.
- 26 G. T. S. T. da Silva, K. T. G. Carvalho, O. F. Lopes and C. Ribeiro, *Appl. Catal., B*, 2017, **216**, 70–79.
- 27 P. Chen, P. Xing, Z. Chen, X. Hu, H. Lin, L. Zhao and Y. He, *J. Colloid Interface Sci.*, 2019, **534**, 163–171.
- 28 K. Wang, Y. Li, J. Li and G. Zhang, *Appl. Catal., B*, 2020, **263**, 117730.
- 29 X. Kong, Q. Lu, J. Huang, L. Li, J. Zhang, X. Wang, J. Li, Y. Wang and Q. Feng, *J. Alloys Compd.*, 2018, **746**, 68–76.
- 30 F. Liang, X. Sun, S. Hu, H. Ma, F. Wang and G. Wu, *Diamond Relat. Mater.*, 2020, **108**, 107971.
- 31 M. A. Khan, S. Mutahir, F. Wang, W. Lei, M. Xia and S. Zhu, *J. Hazard. Mater.*, 2019, **367**, 293–303.
- 32 L. X. C. T. Rajh, K. Lukas, T. Liu, M. C. Thurnauer and D. M. Tiede, *J. Phys. Chem. B*, 2002, **106**, 10543–10552.
- 33 S. Li, C. Wang, M. Cai, F. Yang, Y. Liu, J. Chen, P. Zhang, X. Li and X. Chen, *Chem. Eng. J.*, 2022, **428**, 131158.
- 34 J. Bai, R. Shen, W. Chen, J. Xie, P. Zhang, Z. Jiang and X. Li, *Chem. Eng. J.*, 2022, **429**, 132587.
- 35 Y. Zhu, E. Li, H. Zhao, S. Shen, J. Wang, Z. Lv, M. Liu, Y. Wen, L. Lu and J. Liu, *Surf. Interfaces*, 2021, **25**, 101262.
- 36 Y. Yang, Z. Zeng, G. Zeng, D. Huang, R. Xiao, C. Zhang, C. Zhou, W. Xiong, W. Wang, M. Cheng, W. Xue, H. Guo, X. Tang and D. He, *Appl. Catal., B*, 2019, **258**, 117956.
- 37 S. Li, G. Dong, R. Hailili, L. Yang, Y. Li, F. Wang, Y. Zeng and C. Wang, *Appl. Catal., B*, 2016, **190**, 26–35.

